Molecular dysregulation of ciliary polycystin-2 channels caused by variants in the TOP domain

Thuy N. Vien[a,1], Jinliang Wang[b,1], Leo C. T. Ng[a], Erhu Cao[b], and Paul G. DeCaen[a,2]

[a]Department of Pharmacology, Feinberg School of Medicine, Northwestern University, Chicago, IL 60611; and [b]Department of Biochemistry, University of Utah School of Medicine, Salt Lake City, UT 84112

Edited by Richard W. Aldrich, The University of Texas at Austin, Austin, TX, and approved March 24, 2020 (received for review November 26, 2019)

Genetic variants in *PKD2* which encodes for the polycystin-2 ion channel are responsible for many clinical cases of autosomal dominant polycystic kidney disease (ADPKD). Despite our strong understanding of the genetic basis of ADPKD, we do not know how most variants impact channel function. Polycystin-2 is found in organelle membranes, including the primary cilium—an antennae-like structure on the luminal side of the collecting duct. In this study, we focus on the structural and mechanistic regulation of polycystin-2 by its TOP domain—a site with unknown function that is commonly altered by missense variants. We use direct cilia electrophysiology, cryogenic electron microscopy, and superresolution imaging to determine that variants of the TOP domain finger 1 motif destabilizes the channel structure and impairs channel opening without altering cilia localization and channel assembly. Our findings support the channelopathy classification of *PKD2* variants associated with ADPKD, where polycystin-2 channel dysregulation in the primary cilia may contribute to cystogenesis.

ion channels | polycystic kidney disease | structural biology | TRP channels | ADPKD

Autosomal dominant polycystic kidney disease (ADPKD) is the most common heritable form of kidney disease (1). The disease is characterized by the development of numerous kidney cysts that often cause renal failure in midlife (2). Approximately 95% of cases of ADPKD are associated with variants in polycystin genes, *PKD1* or *PKD2,* which encode for polycystin-1 and polycystin-2, respectively (3, 4). Individuals with ADPKD often carry germline variants in one allele and the midlife disease onset is attributed to the acquisition of a second somatic mutation in the remaining allele in cystic cells (5, 6). Polycystin-2 is a member of the RCSB protein data bank (TRPP) class of ion channel subunits which contain six transmembrane spanning helices (7). Polycystin-1 is a membrane protein with 11 transmembrane spanning helices that is related to adhesion class G protein-coupled receptors and TRPP channels. Based on biochemical analysis and immunolocalization results, polycystin-1 and polycystin-2 can form a complex that traffics to the primary cilia of kidney collecting duct epithelia (3, 4, 8). Primary cilia are microtubule-based organelles that extend from the apical side of cells and amplify critical second messenger pathways (9–11). While two groups have independently verified that polycystin-2 is required for channel formation in the primary cilia, the contribution of polycystin-1 to the voltage-dependent, large-conductance cilia current appears to be dispensable (12, 13). However, this work does not exclude the possibility that the polycystin-1 and -2 complex is biologically relevant. Indeed, cryogenic electron microscopy (cryo-EM) structures have captured polycystin-2 in its homomeric form and in complex with polycystin-1 (14–17). Recent work expressing *PKD1* with *PKD2* genes demonstrates that ion selectivity can be altered when polycystin-1 is incorporated, but this only occurs when polycystin-2 is trapped in an open state by mutations in pore residues (18). Thus, these results do not discern if polycystin-1 is operating as a chaperone for polycystin-2 or forms a bona fide ion channel with undetermined gating properties. Since the native form of the putative heteromeric channel has escaped detection, we have focused our efforts on determining the impact of ADPKD-causing variants within the context of the homomeric polycystin-2 ion channel.

For more than 20 y, variants in polycystins have been implicated in ADPKD, yet our understanding of their impact on channel function and biosynthesis is insufficient. Cells isolated from ADPKD cysts often contain premature stop codons, or large truncations or insertions in *PKD1* or *PKD2* (19, 20). These drastic alterations suggest that ADPKD is caused by a loss-of-polycystin function (19). This hypothesis is supported by results of rodent models of ADPKD in which haploinsufficiency and loss of heterozygosity of *PKD1* or *PKD2* cause kidney cyst formation in mice (21). Although there are currently no mouse models harboring human disease-causing *PKD2* variants, human *PKD2* transgene expression can dose-dependently rescue the ADPKD phenotype in *PKD2* null mice (22). Two clinically relevant *PKD2* missense variants—D511V and T721A—cause a complete loss of channel activity when measured using reconstitution assays from endoplasmic reticulum (ER) membranes (23). However, using this method we learned little about how variants disrupt polycystin-2 channel mechanics and cellular localization. Paradoxically, there is evidence that transgene overexpression of *PKD2* may also cause the polycystic kidney

Significance

How do variants that cause autosomal dominant polycystic kidney disease (ADPKD) alter the structure and function of polycystin-2 channels? This 20-y-old question remains unanswered because polycystins traffic to organelle membranes, such as the primary cilia, that are challenging locations to study. Here, we focus on the molecular impact of variants found in the TOP domain of polycystin-2, a site commonly mutated in ADPKD. We report the C331S variant structure, where the TOP domain is destabilized by the localized mutation. We find that TOP domain variant channels still assemble but fail to open at normal voltages. Importantly, these variant channels retain their native primary cilia trafficking, suggesting their availability to drug modulators as a rationale for ADPKD treatment.

Author contributions: P.G.D. designed research; T.N.V., J.W., L.C.T.N., and P.G.D. performed research; T.N.V., J.W., L.C.T.N., and P.G.D. contributed new reagents/analytic tools; T.N.V., J.W., L.C.T.N., E.C., and P.G.D. analyzed data; and T.N.V., E.C., and P.G.D. wrote the paper.

The authors declare no competing interest.

This article is a PNAS Direct Submission.

This open access article is distributed under Creative Commons Attribution-NonCommercial-NoDerivatives License 4.0 (CC BY-NC-ND).

Data deposition: The polycytsin-2 C331S variant molecular structure coordinates derived from the cryogenic electron microscopy datasets have been deposited in the RCSB Protein Data Bank, https://www.rcsb.org/ (code 6WB8) and Electron Microscopy Data Bank, https://www.ebi.ac.uk/pdbe/ (code EMD-21586).

[1]T.N.V. and J.W. contributed equally to this work.

[2]To whom correspondence may be addressed. Email: Paul.Decaen@northwestern.edu.

This article contains supporting information online at https://www.pnas.org/lookup/suppl/doi:10.1073/pnas.1920777117/-/DCSupplemental.

First published April 24, 2020.

www.pnas.org/cgi/doi/10.1073/pnas.1920777117

phenotype in mice (24). Furthermore, human *PKD2* overexpression in mice leads to abnormalities in tubule development and eventual kidney failure (25). Thus, the biophysical mechanism by which ADPKD variants may cause a loss of function or a gain of function of polycystin-2 is debatable and highlights the present need to assess their impact on channel gating, structural assembly, and localization to the ciliary membrane.

The published polycystin-2 cryo-EM structures provide atomic maps for locating ADPKD variants and a framework for hypothesis generation of the structural regulation of this channel (14–17). We reported that the homotetrameric polycystin-2 TOP domains (also called the "polycystin domains") interlock to form a unique lid-like structure that engages the channel pore from the external side (17). More than 80% of the reported missense variants identified in ADPKD patients (https://pkdb.mayo.edu/) can be mapped onto the TOP domain (26). Since the TOP domain (~220 residues) represents a novel fold found only in polycystin proteins, it is difficult to speculate how this structure may regulate channel biophysics and biosynthesis. Based on structural observations, we propose two competing—but not mutually exclusive—mechanistic hypotheses regarding the impact of these variants. First, the TOP domain forms a molecular bridge between the voltage sensor domain (VSD) and the ion-conducting pore domain (PD). Here, the TOP is well positioned to transfer voltage-dependent conformational changes in the VSD to open the channel pore, and we hypothesize that TOP domain variants will disrupt polycystin-2 channel gating. Second, the TOP domain also forms homotypic contacts between each subunit, which likely stabilize the oligomeric channel structure. Since there is strong precedence for external domains' being essential for tetrameric ion channel formation and native membrane localization, we hypothesize that TOP domain variants may disrupt the channels' structure, assembly, and trafficking to the primary cilia (27–29). Thus, the effect of ADPKD mutations found in the TOP domain forms the basis of the present study.

Located within the TOP domain, the finger 1 motif is the site of five highly pathogenic, germline missense variants (K322Q/W, R325Q/P, and C331S) in the human ADPKD population. In the present study, we report the cryo-EM structure of the C331S variant, which distorts the structure of the finger 1 motif and the TOP domain. Despite these changes in atomic structure, C331S and the other finger 1 variants do not alter polycystin-2 channel assembly and localization to the cilium as visualized through superresolution microscopy. However, all five variants cause a loss of ion channel function as measured by voltage clamping the primary cilium membrane. We report that analogous mutations in the related polycystin-2L1 (*PKD2-L1*) channels cause a loss of function, demonstrating that the conserved interactions are necessary for the function of TRPP subfamily members. Based on our previously published cryo-EM structure of polycystin-2, we know the C331 variant site participates in a disulfide bond found within finger 1 of the TOP domain (17). We report that breaking the finger 1 disulfide bond, either by mutation or chemical reduction, causes disorder in the TOP domain and facilitates channel closure by shifting the voltage dependence to depolarizing potentials. This work identifies the molecular dysregulation of polycystin-2 channels that underlies forms of ADPKD caused by finger 1 motif variants in *PKD2*. Our results demonstrate that the TOP domain is essential for voltage-dependent gating but that sites found within the finger 1 motif do not alter channel assembly and ciliary trafficking.

Results

Proposed Atomic Interactions Disrupted by ADPKD-Causing Variants in TOP Domain's Finger 1 Motif. Previously, the polycystin-2 homotetrameric structure embedded in lipid nanodiscs was solved at 3-Å resolution using single-particle cryo-EM (17). Here, we described the TOP domain (also called the "polycystin domain" in the initial publication) which forms an extracellular, lid-like structure in which >80% ADPKD-causing *PKD2* missense variants are found. The TOP domain (residues 242 to 468 between the S1 and S2 helices) forms a novel protein fold composed of three α helices and a five-stranded antiparallel β-sheet which together form two intersubunit interaction motifs called finger 1 and finger 2 (Fig. 1*A* and *SI Appendix*, Fig. S1*A*). Finger 1 is formed by a hairpin turn and interfaces extensively with the β-turn protruding from the adjacent TOP domain. Within finger 1, a disulfide bond is found between the sulfur atoms of C331 and C344 which we hypothesize provides structural integrity to the hairpin and is necessary for its interaction with the adjacent TOP domain (Fig. 1*A* and *SI Appendix*, Fig. S1*A*) (17). C331S is an ADPKD-causing variant whose hydroxyl side chain is unable to form the disulfide bond with C344. Finger 1 extends from the palm of the TOP domain which is composed of the central antiparallel β-sheet and is stabilized by a hydrogen bond network involving Q323–T419–R325 and a cation-π interaction formed between R322–F423 (Fig. 1*A*). Importantly, multiple

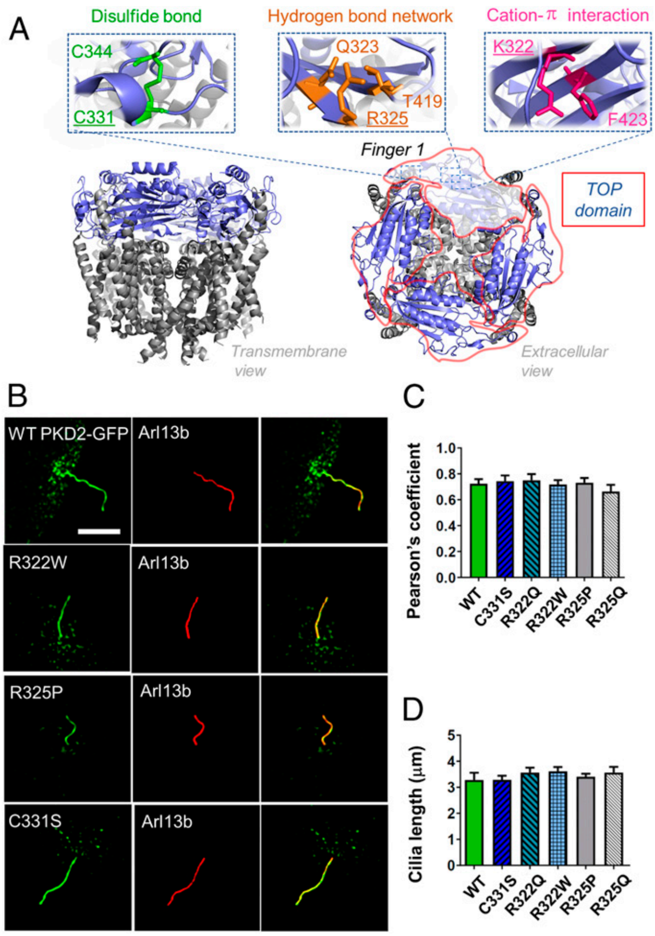

Fig. 1. The atomic interactions disrupted by TOP domain finger 1 motif variants and their impact on cilia localization. (*A*) The location of the TOP domain (blue) structure of the polycystin-2 channel (Protein Data Bank ID code 5T4D). Expanded view of the interactions made by three pathogenic variant sites (underlined) within the finger 1 motif. (*B*) Superresolution SIM (scale bar, 3 μm) images of HEK *PKD2*^{Null} cells stably expressing variants of PKD2-GFP (green) immunolabeled with anti-ARL13B antibody (red). (*C*) Cilia fluorescence colocalization analysis using Pearson's correlation coefficient. (*D*) Comparison of cilia length from the indicated HEK cell lines. Student's *t* test results (*Methods*) comparing WT and variants channels (N.S., $P > 0.05$). The number of cells tested is indicated in parentheses and error bars are equal to SD.

ADPKD-causing missense mutations are found at positions R322 (R322Q and R322W) and R325 (R325Q and R325P) (26). We hypothesize that these pathogenic mutations would destabilize the intersubunit interactions required for channel assembly and may disrupt polycystin-2's native cilia localization. On the other hand, these variants may destabilize the central antiparallel β-sheet of the TOP domain, which oligomerizes and engages the pore on the extracellular side of the channel, altering the channel's ability to gate (open and close).

TOP Domain Finger 1 Variants Do Not Alter Ciliary Trafficking. Contrary to initial reports, expression or coexpression of *PKD1* and *PKD2* does not produce ionic currents on the plasma membrane of native collecting duct cells or in heterologous systems. As characterized previously, we established a method to test heterologous C-terminally green fluorescent protein (GFP)-tagged *PKD2* (PKD2-GFP) channel trafficking and function to the cilia membrane of HEK cells (13). We have improved this system by genetically ablating the endogenous *PKD2* expression in our HEK cell line ($PKD2^{Null}$) using the CRISPR/Cas9 method (clustered regularly interspaced short palindromic repeats) so that the impact of variants can be assessed without the contribution of endogenous alleles (*SI Appendix*, Fig. S1*B*). Then, we stably introduced PKD2-GFP to observe its subcellular distribution using structured illumination microscopy (SIM; *SI Appendix*, Fig. S2*A*). SIM axial resolution is ∼150 nm, which is twice that of confocal microscopy and enables a more detailed view of the primary cilium, which is less than 400 nm in diameter (30). Here, PKD2-GFP trafficked to the $PKD2^{Null}$ cell primary cilia, as assessed by GFP colocalization with antibodies raised against epitopes ADP ribosylation factor-like GTPase 13B (ARL13B), adenylate cyclase 3 (AC3), and acetylated tubulin (AT) (*SI Appendix*, Table S2). Analyses of these images indicate that PKD2-GFP signal had the highest Pearson's coefficient with ARL13B, and thus we used this marker as a benchmark to assess the effects of ADPKD variant effects on polycystin-cilia localization (*SI Appendix*, Fig. S2*B*). We generated six stable cell lines expressing the uncharacterized finger 1 variants (R322Q, R322W, R325Q, R325P, and C331S). However, none of the variants impacted primary cilia trafficking or length when compared to the wild-type (WT) channel (Fig. 1 *C* and *D*), demonstrating that the TOP domain mutations do not alter cilia maintenance or the channel's native localization in the cell.

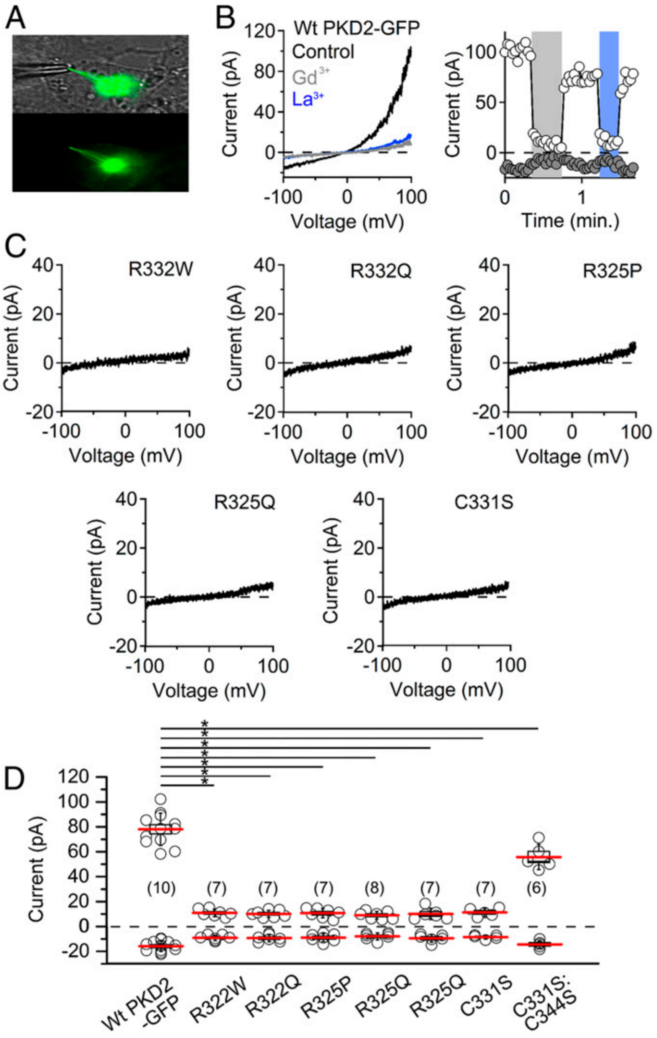

Fig. 2. Finger 1 variants cause of loss-of-channel function in the primary cilia. (*A*) Image of a voltage-clamped primary cilium from a HEK $PKD2^{Null}$ cell stably expressing WT PKD2-GFP. Note that the GFP signal is present in the primary cilium and that the patch electrode is sealed onto cilia membrane. (Scale bar, 5 μM.) (*B*, *Left*) Exemplar ciliary WT polycystin-2 currents activated by voltage ramps and blocked by 10 μM lanthanum (La^{3+}) or gadolinium (Gd^{3+}). (*B*, *Right*) The time course of outward (100 mV) and inward (−100 mV) current block by trivalent ions. (*C*) Lack of ciliary current measured from HEK cells expressing TOP domain variants. (*D*) Box (mean ± SEM) and whisker (mean ± SD) plots of cilia total outward (100 mV) and inward cilia (−100 mV) current measured from HEK cilia expressing the indicated channels. Number of cilia for each channel is indicated in parentheses. Resulting P values < 0.05 from Student's t-test values comparing the outward currents from WT and variants are indicated by an asterisk.

Finger 1 Variants Cause a Loss of Channel Function in the Primary Cilia. Next, we sought to determine if the variants alter polycystin-2 channel activity in the primary cilia and ER membranes. Since the WT channel and the finger 1 variants did not alter PKD2-GFP cilia localization, we could thus visualize the HEK cilia to establish electrophysiology recordings of the channels directly from the cilia membrane, as previously reported (Fig. 2*A*) (13). Here, the heterologous WT channel PKD2-GFP cilia current is outward-rectifying when activated by voltage ramps and is blocked by external trivalent ions gadolinium and lanthanum—matching the pharmacology observed in native polycystin-2 currents measured from pIMCD cilia (Fig. 2*B*) (13). However, the recordings from the cilia of all five variant cell lines resulted in an apparent loss of polycystin-2 current (Fig. 2 *C* and *D*). Evidently, finger 1 variants disrupt channel gating in the primary cilium without effecting its ciliary trafficking. Since the primary cilia is absorbed or shed during active cell mitosis, *PKD2* expression is primarily confined to the ER during this nonciliated stage of cell division (31, 32). Indeed, the ER population of polycystin-2 channels localized with the ER membrane when immunolabeled with ER-tracker (*SI Appendix*, Fig. S3*A*). Previous work using cytoplasmic Ca^{2+} fluorescence dyes supports the hypothesis that polycystin-2 can function as a Ca^{2+} store–release channel in the ER, potentiating the response of the inositol trisphosphate receptor (InsP3R) in kidney collecting duct cells (19). To determine if our variants alter the activity in the ER-localized polycystin-2 population, we activated the endogenous muscarinic acetylcholine receptor M1 (M1R) and assayed (50 μM) carbachol stimulation of the InsP3R-mediated Ca^{2+} store release using the cytoplasmic ratiometric calcium indicator, Fura-2 (*SI Appendix*, Fig. S3*B*). However, we did not observe any difference in carbachol-mediated Ca^{2+} release from intracellular stores of $PKD2^{Null}$ cells or when PKD2-GFP was stably overexpressed (*SI Appendix*, Fig. S3 *C* and *D*). In addition, there was no difference in the Ca^{2+} store release kinetics and maximal response between cells stably expressing WT and the TOP domain variant channels (*SI Appendix*, Fig. S3 *C* and *D*). We also tested calcium responses elicited from a lower dose of

BIOPHYSICS AND COMPUTATIONAL BIOLOGY

carbachol (3 μM) in cells expressing endogenous M1R and when the receptor was overexpressed (*SI Appendix* and see *SI Appendix*, Fig. S4 *A* and *B*). Again, no difference was observed from parental HEK cells, *PKD2*^{Null} cells and *PKD2*^{null} cells overexpressing PKD2-GFP. Since our results using this method did not reproduce polycystin-mediated potentiation of Ca^{2+} store release reported in native cells (*Discussion*), we directed our remaining experiments toward understanding how these variants impact polycystin-2 activity from the primary cilia membranes.

Finger 1 Variants Impair Voltage-Dependent Gating. To examine the biophysical mechanisms which cause loss of function observed in the five finger 1 variants, we recorded single channel currents in the "on-cilia" patch configuration at potentials up to 160 mV (Fig. 3 *A* and *B* and *SI Appendix*, Fig. S5). Here we observed that the voltage dependence of channel opening ($V_{1/2}$) for all of the variant channels was positively shifted by 87 mV or more compared to WT channels. Results from the single-channel recordings explains the lack of whole-cilia current measured by depolarizing voltages tested to 100 mV, because the threshold to activate the finger 1 variant channels is more depolarized. We did not observe a significant difference in the single-channel conductance between the WT and the variant channels, indicating that the pore properties were unaltered (Fig. 3*C*). Next, we tested the effects of chemically breaking the finger 1 C331–C344 disulfide bond in real time while recording polycystin-2 currents in the "whole-cilia" configuration. We applied external disulfide reducing agents Tris-2-carboxyethyl phosphine (TCEP) or reduced glutathione (GSH) and observed near-instantaneous reduction in the WT polycystin-2 current that was readily reversible (Fig. 4*A*). TCEP and GSH were selected because they are membrane-impermeable, having octanol:water partition coefficients of −4.9 and −4.7, respectively, and could only reduce the extracellular accessible disulfide bonds. Since the ADPKD-causing variant C331S causes a loss-of-channel function, we proposed that mutating its disulfide interacting partner, C344, would have a similar effect. Serine was substituted for C344 because its side-chain hydroxyl has a volume similar to cysteine sulfhydryl atoms, and thus this substitution would likely be tolerated at this position but incapable of forming a disulfide bond. As expected, stably expressing C344S failed to produce cilia currents (Fig. 4*B*). While these results implicate the sites as important for polycytin-2 functions they do not demonstrate that their interaction is required for their function. Thus, we introduced an artificial hydrogen bond interaction at these positions to see if it would rescue the cilia current. We replaced both positions C331 and C344 with serine within the same channel (C331S:C334S). Now, the native interacting sulfhydryl side chains are replaced with hydroxyl residues that can form a hydrogen bond that is not dependent on redox conditions. As expected, C331S:C334S channel generates a functional cilia current which is resistant to antagonism by external reducing agents, while retaining its sensitivity to pore block by gadolinium (Fig. 4 *C* and *E*). The results from this rescue experiment demonstrate that an interaction at this site, disulfide or a hydrogen bond, is necessary for polycystin gating. However, the effect of the antagonism of polycystin-2 by reducing agents could be attributed to hydrolysis to other cysteine pairs within the channel. While there are two other extracellularly located cysteine residues found in polycystin-2 (C437 and C632), neither of these resides participate in disulfide bonds. C437 resides in the fourth strand of the antiparallel β-sheet of the TOP domain and C632 are found in the lipid-facing side of the first pore helix (P1; *SI Appendix*, Fig. S1*A*). We substituted both positions with serine resides by generating a C437S:C632S double-mutant channel and found that the double-mutant channel remained functional in the cilium and retained its sensitivity to GSH and TCEP—thus eliminating the possibility that these are responsible for the observed effect (Fig. 4 *D* and *E*). Taken together, we conclude that breaking C331–C344 interaction either by chemical reduction or sulfhydryl substitution results in a loss of polycystin-2 channel function by shifting the channels' voltage dependence to depolarizing potentials.

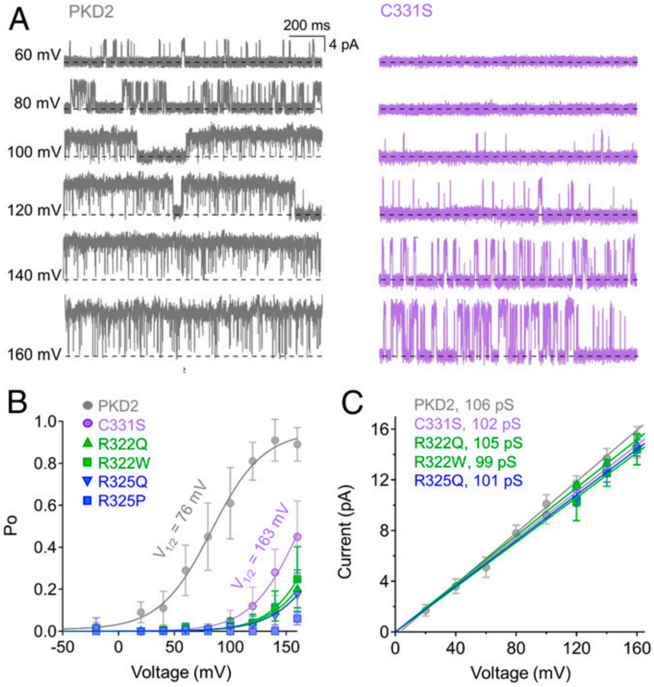

Fig. 3. Finger 1 variants shift voltage-dependent opening of polycystin-2. (*A*) Exemplar single-channel recordings measured from the cilia of HEK *PKD2*^{Null} cells expressing WT or C331S polycystin-2 channels. (*B*) Average channel open probability plotted as a function of voltage. The data were fit to a Boltzmann equation to estimate the half maximal voltage response ($V_{1/2}$) and the slope factor (Z), which was used to calculate the free energy required to open the channels (ΔG°; see *Methods* for equation). (*C*) Average single-channel current amplitudes. Conductance (γ) estimated by fitting the average single channel currents to a linear equation. Error bars indicate SD from six cilia recordings from each cell type.

Conserved TOP Domain Molecular Interactions Are Required for Polycystin-2L1 Gating. Heterologous expression of *PKD2L1* encodes for functional polycystin-2L1 ion channels in the plasma membrane, whereas *PKD2* does not (33). Previously, we reported expression of *PKD2L1* is required for the ciliary conductance of nonrenal cells (e.g., retina pigmented epithelia cells), whereas *PKD2* is required for cilia current recorded from kidney tubule epithelial cells. Thus, while both polycystin-2 and polycystin-2L1 can form ion channels in primary cilia, their cilia expression and localization are dependent on tissue type. Based on sequence alignments and structural analysis of the cryo-EM structures of polycystin-2 and polycystin-2L1, the finger 1 variant sites and their contributing interactions are conserved in both channels (*SI Appendix*, Figs. S1*A* and S5) (34, 35). Therefore, we tested polycystin-2L1 channel mutations R201Q, R201W, K204Q, K204P, and C210S—which are equivalent to the R322Q, R322W, R325Q, R325P, and C331S variants in the polcystin-2 channel, respectively. Transient overexpression of *PKD2L1* (polycystin-2L1) generates an outwardly rectifying current in the plasma membrane that is sensitive to trivalent block (*SI Appendix*, Fig. S6*B*). However, introducing any one of the finger 1 variants resulted in a complete loss of the current (*SI Appendix*, Fig. S6 *C–E*). These findings suggest these TOP domain finger 1 interactions are required for both polycystin channel types. The finger 1 disulfide of polycystin-2L1 is formed between residues

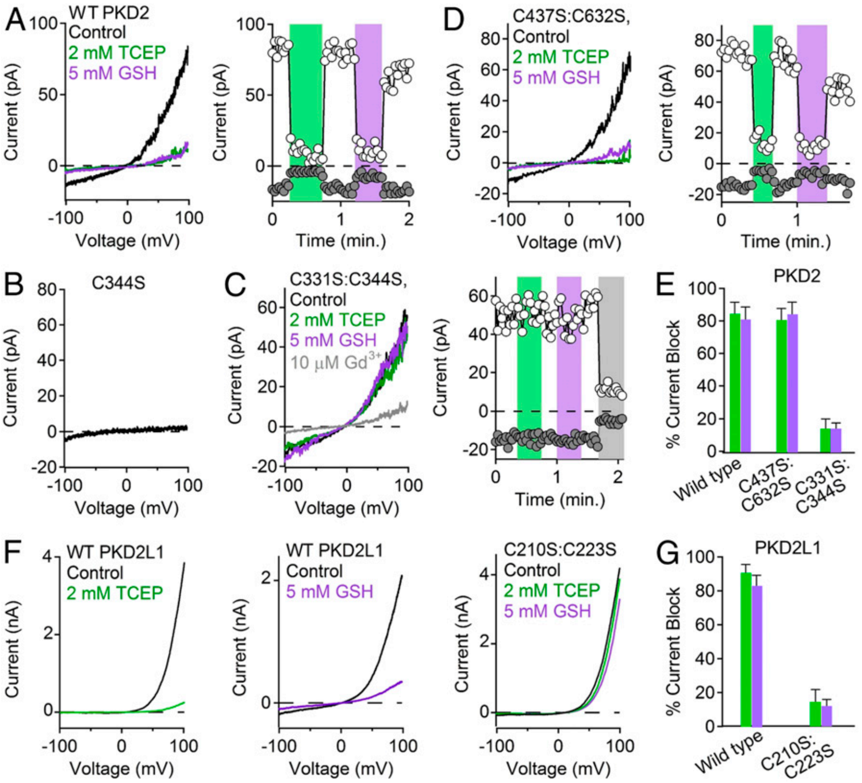

Fig. 4. The finger 1 disulfide bond is required for polycystin-2 and polycystin-2L1 gating. (*A*–*D*, *Left*) Exemplar currents activated by voltage ramps measured from the primary cilia of HEK cells stably expressing the indicated polycystin-2 channels under control and reducing conditions. (*A*–*D*, *Right*) The time course of inward (−100 mV) and outward (100 mV) current block by reducing agents and gadolinium. (*E*) Bar graph showing the average percent block of outward polycystin-2 currents by TCEP (green) and GSH (purple). $n = 5$ cells and error bars are equal to SD. (*F*, *Left*) Exemplar whole-cell polycystin-2L1 currents activated by voltage ramps and their block by reducing agents. (*F*, *Right*) The time course of current block. (*G*) Bar graph showing the average percent block of outward polycystin-2L1 currents by the reducing agents. $n = 6$ cells and error is SD.

C210 and C223, and substituting either cysteine results in a loss of channel function—echoing results from the polycystin-2 channel (*SI Appendix*, Fig. S6*C*) . As done for the ciliary polycystin-2 channels, we chemically reduced the polycystin-2L1 finger 1 disulfide bond by applying the extracellular TCEP or GSH and observed a near-complete loss of current, which was readily reversible (Fig. 4*F*). Replacing the finger 1 disulfide interaction with a hydrogen bonding pair, C210S:C223S, partially restored its conductance and rendered the channel insensitive to GSH (Fig. 4 *F* and *G* and *SI Appendix*, Fig. S6*E*). The results from the polycystin-2L1 channels recapitulate our polycystin-2 findings, where an interaction at these sites within finger 1 is required to open the channel.

Destabilization of the TOP Domain in the Cryo-EM C331S Variant Channel Structures. To determine if disrupting TOP domain interactions alters channel assembly and stability, we expressed and purified the C331S variant of polycystin-2 (residues 53 to 792) protein in amphipols for structural determination using single particle cryo-EM. Two-dimension (2D) class averages showed a broad distribution of views in which the distinct channel features of the tetrameric architecture are clearly discernible (*SI Appendix*, Fig. S7). Thus, the C331S mutation did not substantially impair the channel's quaternary structure. Nevertheless, further in silico three-dimensional (3D) classification revealed two populations of particles (*SI Appendix*, Fig. S8). The first structure class is refined to 3.24 Å and essentially superimposes with the WT channel, except lacking the disulfide bond. Surprisingly, breaking the disulfide bond only slightly altered the finger 1 hairpin (Fig. 5 *A* and *B* and *SI Appendix*, Fig. S9*A* and Table S1). The second class retained the tetrameric architecture as well, but the TOP domain was visibly disordered (*SI Appendix*, Fig. S8). It is important to note that we have not observed this disorder in the WT or the previously reported F604P structures, even though the data-processing procedures were the same (17, 36). We also considered that the C331S variant may break fourfold symmetry, but refinement of this second class without imposing any constraints still yielded a map with the same C4 symmetry. Using size-exclusion chromatography, we observed that polycystin-2 is stable at temperatures beyond 50 °C (Fig. 5 *C* and *F*) in DDM (*n*-dodecyl β-D-maltoside) detergent. Since chemical reduction of the polycystin-2 inhibited the ciliary current, we added GSH to our purification conditions and observed channel protein denaturing at lower temperatures, suggesting that reduction of the sole disulfide bond between C331S–C344 disrupts the channel stability (Fig. 5 *E* and *F*). Similarly, approximately half the C331S variant protein denatured when the sample was heated to 50 °C, generating more monomeric subunits in the process (Fig. 5 *D* and *F*). Our data demonstrate that the C331S variant causes subtle differences within the finger 1 structural fold but leads to destabilization of the overall TOP domain and channel function. We did not observe appreciable alterations to the positions of the transmembrane helices between the variant and WT structures (*SI Appendix*, Fig. S9), as both channels appear to be captured in a closed state. These observations are not surprising given that opening the WT and C331S channels require a positive membrane potential, which is missing from the cryo-EM conditions.

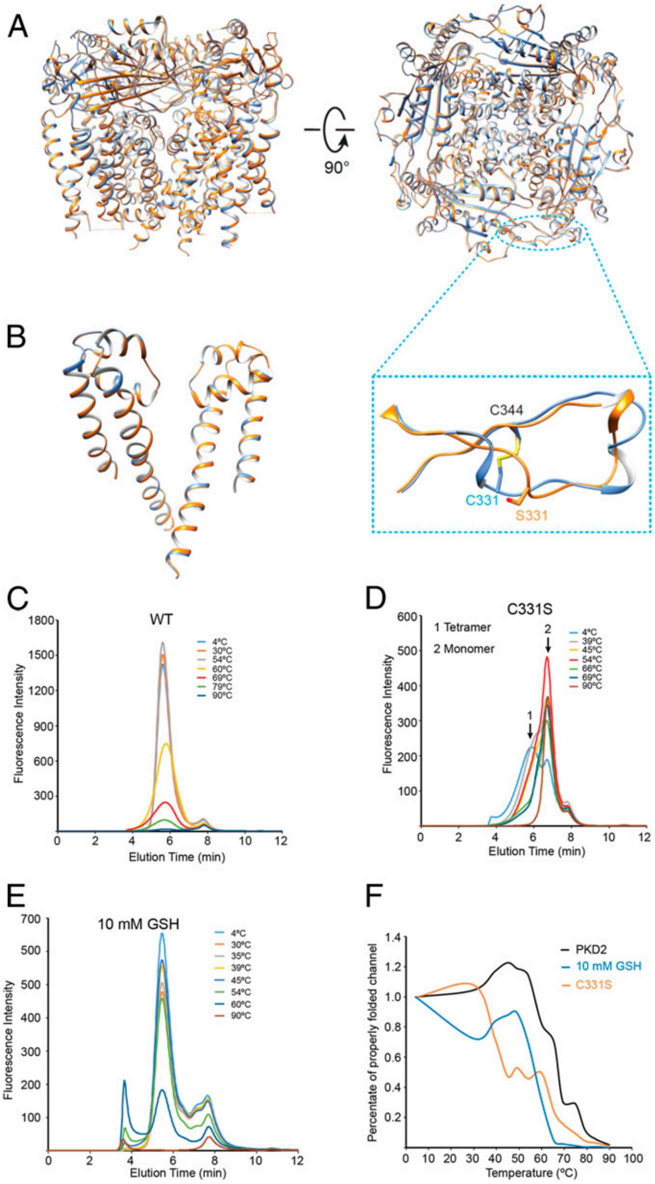

Fig. 5. The C331S variant destabilizes the TOP domain without impairing channel assembly. The 3.4-Å cryo-EM structure of the polycystin-2 C331S variant. (*A*) Transmembrane (*Left*) and extracellular (*Right*) views of the superimposed WT (blue) and C331S (orange) polycystin-2 structures. (*A*, *Inset*) An expanded view of the finger 1 cysteine interactions. (*B*) The pore domain (*SI Appendix*, Figs. S5 and S6) from two subunits of the WT and variant channel structures. Note that there is little difference in the PD structures. (*C*–*E*) Size-exclusion chromatography profiles of the WT channels under neutral and reducing conditions (10 mM GSH) and for the C331S mutant with samples treated at indicated temperatures. (*F*) Thermal de\-nature profiles for WT channels under standard and reducing conditions and for the C331S variant. The C331S and WT channels treated with GSH denature at lower temperature compared to the WT channel in neutral conditions.

Discussion

ADPKD as a Channelopathy. There are more than 400 genes which encode ion channel subunits that control the flux of ions across cell membranes. Ion channels are involved in many physiological processes, including neurotransmission, muscle contraction, secretion, immune response, cell proliferation, and differentiation (37). Variants in genes that encode ion channels or their interacting protein subunits are responsible for many rare and common conditions that impact organ function (38). Collectively, these genetic diseases are called channelopathies and can be debilitating or lethal (39, 40). ADPKD is one of the most common life-threating monogenetic disorders and we have directly demonstrated that five variants impair the polycystin-2 channel function in the primary cilia membrane. Thus, the forms of ADPKD caused by *PKD2* variants support it's categorization as a channelopathy. In mouse models of ADPKD, both overexpression and ablation of *PKD2* can drive the phenotype in mice (21, 24). While most large insertion and truncation variants likely cause a loss of function, the impact of missense variants is uncertain (41). In our study, we focused on one location in polycystin-2 finger 1, where variants destabilize the TOP domain structure. The functional impact is a loss-of-channel function by reducing the channels' open probability via a shift in voltage dependence to positive potentials. Importantly, these channels are still "available" in the cilia membrane and present a rationale for the design of gating modifying drugs that target polycystin-2. Indeed, gating modulation is common mechanism of action in many prototypic therapeutic drugs that target ion channels (42, 43). Our study demonstrates that destabilization of the TOP domain affects channel gating. Therefore, besides gating modifiers which target the VSD, theoretically drugs could be developed to stabilize the TOP domain to achieve the same therapeutic effect. Since the TOP domain is a novel extracellular structural feature of polycystins, it may represent a unique receptor site to achieve drug target specificity. Other missense variants found in the VSD, pore, and cytoplasmic domains may have drastically different consequence on polycystin-2 activity. Understanding these mechanistic differences from patients with unique variants may provide a rationale for the development of personalized medicine for the treatment of ADPKD.

The TOP Domain's Molecular Regulation of Polycystin-2. At the outset of this work, we proposed that variants in finger 1 might alter polycystin-2 activity by impairing channel opening, or assembly and trafficking to the primary cilia. Our study clearly demonstrates that these variants disrupt the stability of the TOP domain and impair channel gating without impacting channel cilia localization. Disrupting the disulfide interaction within finger 1—either by mutations or chemical reduction—results in a shift in the voltage dependence of polycystins (polycystin-2 and polycystin-2L1), enhancing the closure rate and doubling the amount of free energy required to open channels. This result prompts us to ask: What is the mechanistic model for how the TOP domain controls channel opening? We propose that the TOP domain may structurally gate this channel in one of two ways. First, it may serve as a fixed point from which the transmembrane portions of the channel move in response to changes in membrane potential and it transfers the motion to open the channel gate(s). In this model, the TOP domain–VSD interaction is structurally reminiscent of how spider toxins engage the VSD of voltage-gated sodium and potassium channels, restricting motion of the VSD and trapping them in conducting or nonconducting states (44, 45). Alternatively, the TOP domain itself may move in response to activation of the VSD, transferring the motion of the VSD to the opening of the channel's proposed upper gate. Both gating models appear to be structurally plausible, and additional biophysical studies are required to determine which mechanism is most valid.

Implications for ADPKD Classification as a Ciliopathy. Nearly all gene variants implicated in inherited human cystic kidney diseases impact proteins that localize to the primary cilium or basal body and are usually accompanied by abnormal ciliary signaling (46, 47). These diseases are categorized as renal ciliopathies due to their phenotypic convergence and subcellular localization of the impacted protein. Although not conclusive, ADPKD is commonly categorized as a renal ciliopathy. In this paper, we measured the biophysical dysregulation caused by polycystin-2 mutations associated with ADPKD directly from the primary cilia—which supports the classification of ADPKD as a ciliopathy. This view is supported by two independent electrophysiology studies which measured polycystin-2's Ca^{2+} conductance in collecting duct primary cilia. Thus, Ca^{2+} dysregulation in the cilia is likely a direct consequence in ADPKD (12, 13). Cells deficient in *PKD2* are reported to have aberrant cytoplasmic calcium, a common signaling mechanism reported for other channelopathies (48, 49). However, the primary cilium has its own resting Ca^{2+} concentration (580 nM) and changes in ciliary Ca^{2+} are demonstrably restricted to this compartment (50). In a recent study, flooding the ciliary compartment with millimolar Ca^{2+} did not affect levels found in the cytoplasm (51). This result is supported by volumetric comparisons of cilia and the cell body, where the cilioplasmic volume of Ca^{2+} (<1 fL) is too small to alter the global cytoplasmic Ca^{2+} concentration (2 to 5 pL) (52). This might explain why no difference in resting cytoplasmic Ca^{2+} was observed when *PKD2* was overexpressed or genetically ablated in our HEK cells. Because of their local enrichment in the cilia, we propose that *PKD2*-mediated Ca^{2+}-dependent signaling initially activates ciliary and periciliary proteins, such as adenylyl cyclase and PKA, which in turn regulates effectors of the Hedgehog pathway in the cell (53, 54). It is noteworthy that other ciliopathies that impair brain development (such as Joubert syndrome, Bardet–Biedl syndrome, and Alström Syndrome) are often caused by gene variants which encode for downstream Ca^{2+}-signaling second messengers and commonly share polycystic kidney disease as a comorbidity (37, 55, 56). It is possible that aberrant cilia-to-cell signaling downstream of ciliary Ca^{2+} is a unifying mechanism for renal and nonrenal ciliopathies. If this proves valid, future work should address which cilia effectors are involved and how downstream signaling pathways within the cytoplasm are responsible for the cystic kidney phenotype for ADPKD and other renal ciliopathies.

Polycystin-2 Function in Other Membranes. In addition to primary cilia, homoterameric and heteromeric channels containing polycystin-2 are proposed to reside in plasma membranes, ER and mitochondria-associated ER membranes (MAMs) (23, 31, 32, 57, 58). However, it is unknown which, or if all, of these channel populations are involved in ADPKD progression. Conditional genetic ablation of *PKD2* abolished the voltage-dependent, outwardly rectifying current measured from primary cilia of cyst-forming kidney collecting duct cells and demonstrated that these channels are functional in this organelle (12, 13). However, cationic currents measured from the plasma membrane of these cells were unaltered. As initially reported, heterologous coexpression of *PKD1* and *PKD2* conducted a nonselective current with no voltage dependence (ohmic) in the plasma membrane of Chinese hamster ovary cells (31). However, this work has proven difficult to reproduce, and subsequent work has drawn into question polycystin-2 function in the plasma membrane (17, 33). It is possible that channels incorporating polycystin-1 + polycystin-2 subunits have unique ion selectivity or have an undetermined gating mechanism which has prevented their detection and characterization (14). However, without determination of the basic gating properties of the putative heteromeric channel its biological function in the cilia or plasma membranes remains an open question.

In this study, we examined InsPR3-mediated Ca^{2+} store release but did not observe differences when *PKD2* was genetically ablated or overexpressed in HEK cells. This result contrasts with the polycystin-mediated Ca^{2+} store release reported in vascular smooth muscle cells and kidney collecting duct cells and suggests that HEK cells are not a good model for these studies (23, 57, 58) Gene expression differences between our cell lines and native cells may explain this divergence in results. The single-channel properties of polycystin-2 measured from the ER and primary cilia membranes contrast significantly (13, 23). Polycystin-2 Ca^{2+} conductance measured from the primary cilium (4 pS) is smaller than those measured from ER reconstitutions (95 pS). Here, membrane composition and channel protein associations may account for these differences. For example, polycystin-2 reportedly forms complexes with resident ER proteins, including InsPR3 (59, 60). In addition, the ER and primary cilia membranes have different phosphoinositide and sphingomyelin compositions (61, 62). The primary cilia membrane has been shown to contain a high level of phosphatidylinositol-4-phosphate established by inositol polyphosphate-5-phosphatase E, which localizes to the base of the cilium, whereas the ER membrane is primarily composed of phosphoinsitide (63, 64). Given that phospholipids have been shown to modulate channel function of other TRP channels, it is possible that lipid differences may modulate in polycystins channels as well (65, 66). The reduced charge of phospholipids in the ER may modulate polycystin-2 gating, as implicated by the lipid occupancy sites found between the VSD and PD of the "multiion state" polycystin-2 structure (15). Thus, polycystin gating behaviors reported from various organelles may have unique characteristics due to differences in membrane lipid compositions.

Redox Regulation of Polycystin-2 through the TOP Domain Disulfide Bond. In this paper, we demonstrate that conductance of polycystin-2 and polycystin-2L1 is regulated by redox potential. What is the physiological relevance for this observation? The proposed intercellular and primary cilia membrane pools of polycystin-2 channels in the kidney are in different redox environments. The lumen of the kidney tubule is an oxidizing environment (oxidizing potential E_0 = 250 to 300 mV)—partly established by the high levels (250 to 500 mM) of uric acid produced by the glomerulus (67)—whereas the lumen of ER (reducing potential $E_0 = -170$ mV) (68, 69) and cytosol ($E_0 = -290$ mV) (70) are in a highly reducing environment, largely due to concentrated GSH (~10 mM) production catalyzed by GSH reductase (71, 72). We demonstrate that polycystin-2 function is abolished by external application of GSH and TCEP ($E_0 = -240$ and -290 mV, respectively) (73, 74). This effect is caused by chemically reducing the C331–C344 finger 1 disulfide bond, which keeps the channel closed. This interaction is conserved in the related polycystin-2L1 channel found in nonrenal cilia and may represent a defining feature of the polycystin subfamily of TRP channels. The redox-inhibition feature might be advantageous to attenuate polycystin channel function intracellularly until it is trafficked to the ciliary membrane. Here, nascent channels would remain closed by GSH reduction of the finger 1 disulfide bond in the cytosolic compartment until they are trafficked to the cilium. Recently, endogenous polycystin-2 has been identified in MAMs and is proposed to facilitate Ca^{2+} transfer between ER and mitochondria (75). Mitochondria respiratory bursts may impact the local redox potential in MAMs through temporal calcium-induced production of reactive oxidation species (76). Future work assessing redox effects on reconstituted polycystin-2 from intracellular membranes would be helpful in determining how this population is physiologically relevant and if it is involved in ADPKD progression.

Methods

Generation of HEK PKD2^{Null} Cell Lines and the Stable Expression PKD2 Variants. To generate the HEK *PKD2*^{Null} cell lines, we used a CRISPR-Cas9 gene editing kit available from Addgene (kit 1000000055). HEK 293 cells were electrotransfected with single-guide RNAs (caccgAGACACCCCCGTGTCCAAAA and aaacTTTTGGACACGGGGGTGTCTc) with the all-in-one Cas9 plasmid. Sequence analysis confirming the homozygous knockout was performed after puromycin selection. Cells generated from single-cell clones were selected after 4 wk of expansion in a 96-well plates. A positive HEK *PKD2*^{Null} clone was verified after extracting the genomic DNA and PCR amplification of the STOP codons with forward (AGCCTCAGGGCACAGAACAG) and reverse (CCACACTGCCCTTCATTGGC) primers. To generate the WT and variant PKD2 GFP or mCherry C-terminally tagged variant cell lines, the hPKD gene was subcloned into lentiviral pLVX-mcherry-N1 (Clontech) or pLVX-GFP-N1 (Clontech) vector using the Gibson assembly method. A linker encoding for six glycine residues was added between the PKD2 gene and the C-terminal tags, and missense variants were generated using standard, site-directed mutagenesis. The third-generation lentiviral packaging plasmids used for stable expression contained pMDLg/pRRE (Addgene), reverse transcriptase pRSV-Rev (Addgene), and envelope-expressing plasmid pMD2.G (Addgene). LentiX-293T cells (Takara) were transfected with polyethylineimine (Polysciences) at a 4:1:1:1 ratio of the transgene and viral packaging constructs. Supernatants were collected 48 and 72 h posttransfection and filtered through a 0.45-μm syringe filter. Lentiviral supernatant was concentrated 100 times using 1 volume of PEG-it (System Biosciences) virus precipitation solution and 4 volumes of lentivirus-containing supernatant. The PEG-it and supernatant mixture were kept at 4° for 24 h and centrifuged at 1,500 rpm for 30 min. The pellet containing lentivirus was resuspended with 1/100th volume of phosphate-buffered saline (PBS) of the original supernatant volume. HEK cells were infected with the lentivirus supernatant; PKD2-GFP or PKD2-mCherry expression was selected using culture media containing puromycin (2 μg/mL) for 30 to 90 d. Cells were then fluorescence-activated cell-sorted (BD FacsMelody) at 5,000 to 10,000 cpm to enrich for the transgene expression. Stable cell lines were cultured in Dulbecco's modified essential medium supplemented with 10% fetal bovine serum and 100 units/mL penicillin, 100 units/mL streptomycin, and 1 μg/mL puromycin selection antibiotic.

Electrophysiology. Ciliary ion currents were recorded using borosilicate glass electrodes polished to resistances of 14 to 22 MΩ using the cilium patch method previously described (33). Whole-cell electrodes used to measure polycystin-2L1 currents were fire-polished to 1.5- to 4-MΩ resistances. Unless otherwise stated, whole-cilia ionic currents were recorded in symmetrical [Na^+]. The pipette standard internal solution contained (in millimolar) 90 NaMES, 10 NaCl, 10 Hepes, and 10 Na4-BAPTA (glycine, *N*, *N′*-[1,2-ethanediylbis(oxy-2,1-phenylene)]bis[*N*-(carboxymethyl)]-,tetrasodium); pH was adjusted to 7.3 using NaOH. Standard bath solution contained 140 NaCl, 10 Hepes, and 1.8 $CaCl_2$, pH 7.4. All solutions were osmotically balanced to 295 (±6) mOsm with mannitol. Extracellular solutions containing TCEP and GSH were used within 6 h of formulation. Data were collected using an Axopatch 200B patch clamp amplifier, Digidata 1440A, and pClamp 10 software. Whole-cilium and excised patch currents were digitized at 25 kHz and low-pass-filtered at 10 kHz. In the whole-cilium configuration, the holding potential was −60 mV and then depolarized using a 400-ms voltage ramp from −100 mV to 100 mV. The whole-cell recordings of polycystin-2L1 currents were either activated by the same ramp protocol or by 100-ms depolarizations to 100 mV from a −100 mV holding potential. External conditions were controlled using a Warner Perfusion Fast-Step (SF-77B) system in which the patched cilia and electrode were held in the perfusate stream. Data were analyzed by Igor Pro-7.00 (Wavemetrics).The polycystin-2 open probability and the polycystin-2L1 tail current–voltage relationships were fit to a Boltzmann function, $f(x) = 1/(1 + \exp[V - V_{1/2}]/k)$ to estimate voltage of half-maximal activation of current ($V_{1/2}$).

Intracellular Calcium Measurements Using Fura-2. Carbachol-mediated intracellular calcium responses were measured from HEK cells expressing endogenous M1R or from cells overexpressing the M1R-mCherry plasmid delivered using the BacMam expression system (Montana Molecular). After 24 h, HEK cells with indicated PKD2 genotypes were seeded onto glass-bottom plates (MatTek Corporation) precoated with poly-L-lysine (Sigma) for 20 h. The cells were incubated for 1 h at 37 °C in complete medium after loading with 2 μg of Fura-2/AM (Invitrogen). The cells were then washed with and stored for 15 min in Tyrode's solution (in millimolar): 140 NaCl, 4 KCl, 2 $MgCl_2$, 2 $CaCl_2$, 10 glucose, and 10 Hepes. Cells were adjusted in pH to 7.4 with NaOH and osmolarity to 300 mOs with D-mannitol. Cells were placed under an inverted wide-field microscope equipped with 20× objective lens (Olympus IX81) and the stage temperature was held at 37C (Tokai Hit). Images of fura-2 fluorescence remission at 520 nm were captured every 2 s during excitation at 320 nm (Ca^{2+}-free) and 340 nm (Ca^{2+}-bound). Images were acquired and analyzed using SlideBook (Intelligent Imaging Solutions), which synchronizes the filter wheel changer (Lambda 10-3; Sutter Instruments) and the camera (ImagEMX2; Hamamatsu). After 40 s in the control solution, 3 μM or 50 μM carbachol was added to the imaging chamber via exchange at rate of 2 to 4 mL/min. Data analysis was performed on Slidebook. Ten to 20 cells were selected from the field of view and their regions of interest of the emission fluorescence from both wavelengths were recorded after subtracting the background fluorescence level; these data were reported as a 340:380 nm ratio. This ratio was averaged at the start (for resting level) and the response was reported after carbachol administration (for maximal response). At least four replicates (N) were performed for each variant. The emission ratios were converted into a measurement of free cytosolic Ca^{2+} concentration using the following equation:

$$[Ca^{2+}] = K_d \cdot \frac{F_{max}}{F_{min}} \cdot \frac{(R - R_{min})}{(R_{max} - R)},$$

where R_{min} and R_{max} is the minimum and maximum experimental emission 340:380 nm ratio, respectively, F_{max} and F_{min} are the 380-nm maximum and minimum fluorescence emission signals at nominal free Ca^{2+} (measured in Tyrode's solution without $CaCl_2$, but with 5 mM EGTA and 20 μM ionomycin added); F_{min} and R_{max} are similar, except at maximal Ca^{2+} level (measured in Tyrode's solution with 10 mM $CaCl_2$ added and 20 μM ionomycin). The Fura-2 and Ca^{2+} dissociation constant was 224 nM, as determined experimentally using a previously described method (77).

Immunocytochemistry, Confocal Microscopy, and SIM. Cells were fixed with 4% paraformaldehyde, permeabilized with 0.2% Triton X-100, and blocked by 10% bovine serum albumin in PBS. Cells and tissue were mounted on glass slides and treated with Fluoshield from Sigma-Aldrich. Detailed information on the type and concentration of primary and secondary antibodies used in this study is listed in *SI Appendix*, Table S2. Confocal images were obtained using an inverted Nikon A1 with a 60× silicon oil immersion, 1.3 numerical aperture objective. Superresolution images using the SIM method were captured under 100× magnification using the Nikon Structured Illumination Super-Resolution Microscope with piezo stepping. Confocal and SIM images were further processed with Fiji ImageJ (National Institutes of Health).

Cryo-EM Data Acquisition. Each 2.5 μL of PKD2 sample at ∼1.5 mg/mL was applied to glow-discharged UltrAuFoil 1.2/1.3 holey 300-mesh gold grids. Grids were plunge-frozen in liquid ethane using a Vitrobot Mark III (FEI) set to 4 °C, 85% relative humidity, 20 s wait time, −1-mm offset, and 2.5 s blotting time. Data were collected on a Krios (FEI) operating at 300 kV equipped with the K2 Summit direct electron detector at Yale University and National Center for CryoEM Access and Training (NCCAT). Images were recorded using SerialEM at Yale or Leginon at NCCAT, with a defocus range between −1.5 and −2.5 μm (78, 79). Specifically, we recorded movies in superresolution counting mode at a magnification of 47,619×, which corresponds to a physical pixel size of 1.05 Å. The data were collected at a dose rate of 1.4 $e^-/Å^2$ per frame with a total exposure of 40 frames, giving a total dose of 59 $e^-/Å^2$.

Image Processing, 3D Reconstruction, and Model Building. Movie frames were aligned, dose-weighted, and then summed into a single micrograph using MotionCor2. Contrast transfer function parameters for micrographs were determined using the program CTFFIND4 (55, 80). An estimated 2,000 particles were manually boxed out in RELION to generate initial 2D averages, which were then used as templates to automatically pick particles from all micrographs. "Junk" particles (i.e., ice contamination and gold support) were manually rejected and all subsequent 2D and 3D processing steps were performed using RELION (56). Specifically, 501,566 particles were initially extracted from 2,143 micrographs and a round of 2D classification (followed by another round of 3D classification) was performed to reject bad particles from downstream analyses. This resulted in a final dataset of ∼74,302 particles that was subsequently used for 3D reconstruction. For 3D classification and refinement, the PKD2 structure (EMD-8354, low-pass-filtered to 60 Å) was used as the starting model with C4 symmetry imposed. RELION autorefinement with C4 symmetry imposed yielded a 3.78-Å resolution map without masking; removing amphipol belt and solvent with a soft mask improved the map to 3.24-Å resolution based on cutoff of gold standard Fourier shell correlation (FSC) = 0.143. The mask was generated in RELION using the relion_mask_create program against the summed two half-maps with options that extend three pixels beyond a preset density threshold of 0.016 and produce a soft edge of three pixels. Local resolution was calculated by RELION. We also carried out reconstruction without imposing any symmetry during 3D classification and refinement steps, and all resulting maps exhibit a rough C4 symmetry except at some disordered loops and the amphipol belt surrounding the transmembrane region of the channels. Since the map calculated with C4 symmetry was better-resolved, we used this map for model building and structural analyses. The map was sharpened with a b factor of −100 $Å^2$ for model building in Coot (81). The model was then refined in real space using Phenix and assessed by Molprobity (*SI Appendix*, Table S1) (82, 83). The FSC curve was calculated between the refined model versus summed half-maps generated in RELION, and resolution was reported at a cutoff of FSC = 0.5. UCSF Chimera was used to visualize and segment density maps, as well as to generate figures (84).

Thermal Stability Assay. Approximately 9 μg of purified human PKD2 channel proteins (WT or C331S) in 30 μL buffer composed of 20 mM Hepes, 150 mM NaCl, 2 mM $CaCl_2$, 0.5 mM TCEP, and 0.5 mM DDM, at pH 7.4, were incubated at 4 °C to 90 °C (4 °C, room temperature, 30 °C, 35.2 °C, 39.3 °C, 44.9 °C, 49 °C, 54 °C, 60 °C, 65.5 °C, 69.4 °C, 75 °C, 79.3 °C, 84 °C, and 90 °C) for 10 min in a thermal cycler. To reduce the C331–C344 disulfide bond in the PKD2 channel, 10 mM GSH was added to all of the buffers during purification and thermal stability assay. The treated channel samples were then diluted 10 times with the same buffer followed by centrifugation for 30 min at 40,000 rpm. Thirty microliters of each cleared channel samples were separated on an analytical size-exclusion column (Superose 6 5/150 GL; GE Healthcare) at 0.3 mL/min flow rate. Proteins were detected by tryptophan fluorescence. The fluorescence-detection size-exclusion chromatography-based thermostability experiments were performed in triplicates for each temperature point. The integrated area of the channel tetramer peak at different temperature points is normalized to that at 4 °C to generate the thermal stability plot.

Statistical Analysis. Statistical comparisons were made using two-tailed Student's t tests using OriginPro software (OriginLab). Experimental values are reported as the mean $\pm$ SEM unless otherwise stated. Differences in mean values were considered significant at $P < 0.05$. All of our results were normally distributed per Shapiro–Wilk Test. The results from Fig. 2 and *SI Appendix*, Figs. S3 and S5 are parametric for all datasets with a P value threshold of 0.1 to reject normalcy.

Data Availability Statement. All cDNA constructs and cell lines used in this study will be available upon request from P.G.D. unless the item(s) are already deposited and available through addgene (https://www.addgene.org/). The polycystin-2 C331S variant molecular structure coordinates derived from the cryo-EM datasets are available through the RCSB Protein Data Bank repository (https://www.rcsb.org/structure/6WB8) and Electron Microscopy Data Bank (https://www.ebi.ac.uk/pdbe/entry/emdb/EMD-21586). The data that support the findings of this study are available from P.G.D. and E.C. upon reasonable request.

ACKNOWLEDGMENTS. We thank Alex Yemelyanov, Pankaj Bhalla, and the expertise of Northwestern University Skin Disease Research Center for their assistance generating the stable cell lines. Some cryo-EM work was performed at the National Center for CryoEM Access and Training and the Simons Electron Microscopy Center located at the New York Structural Biology Center, supported by the NIH Common Fund Transformative High Resolution Cryo-Electron Microscopy program (U24 GM129539) and by grants from the Simons Foundation (SF349247) and New York State. We thank Shenping Wu at Yale University for cryo-EM data collection and the Center for High Performance Computing at the University of Utah for computational support. The following grants were awarded to P.G.D. and funded this work: NIH National Institute of Diabetes and Digestive and Kidney Diseases (1R56DK119709-01, R00 DK106655, 1R01DK123463-01, and NU GoKidney George M. O'Brien Kidney Research Core Center P30DK11485); PKD Foundation Research Grant; Mayo Clinic's PKD Center Pilot and Feasibility Program grant; and Carl W. Gottschalk Research Scholar Grant from the American Nephrology Society. E.C. was supported by NIH grant R01 DK110575, a discovery award (W81XWH-17-1-0158) from the Department of Defense, and a Pew scholar award from The Pew Charitable Trusts.

1. V. E. Torres, P. C. Harris, Y. Pirson, Autosomal dominant polycystic kidney disease. *Lancet* **369**, 1287–1301 (2007).
2. P. A. Gabow, Autosomal dominant polycystic kidney disease. *N. Engl. J. Med.* **329**, 332–342 (1993).
3. T. Mochizuki *et al*., PKD2, a gene for polycystic kidney disease that encodes an integral membrane protein. *Science* **272**, 1339–1342 (1996).
4. J. Hughes *et al*., The polycystic kidney disease 1 (PKD1) gene encodes a novel protein with multiple cell recognition domains. *Nat. Genet.* **10**, 151–160 (1995).
5. M. Koptides, C. Hadjimichael, P. Koupepidou, A. Pierides, C. Constantinou Deltas, Germinal and somatic mutations in the PKD2 gene of renal cysts in autosomal dominant polycystic kidney disease. *Hum. Mol. Genet.* **8**, 509–513 (1999).
6. C. Bergmann *et al*., Polycystic kidney disease. *Nat. Rev. Dis. Primers* **4**, 50 (2018).
7. K. Venkatachalam, C. Montell, TRP channels. *Annu. Rev. Biochem.* **76**, 387–417 (2007).
8. J. L. Brasier, E. P. Henske, Loss of the polycystic kidney disease (PKD1) region of chromosome 16p13 in renal cyst cells supports a loss-of-function model for cyst pathogenesis. *J. Clin. Invest.* **99**, 194–199 (1997).
9. F. Bangs, K. V. Anderson, Primary cilia and mammalian hedgehog signaling. *Cold Spring Harb. Perspect. Biol.* **9**, a028175 (2017).
10. I. A. Drummond, Cilia functions in development. *Curr. Opin. Cell Biol.* **24**, 24–30 (2012).
11. E. C. Oh, N. Katsanis, Cilia in vertebrate development and disease. *Development* **139**, 443–448 (2012).
12. S. J. Kleene, N. K. Kleene, The native TRPP2-dependent channel of murine renal primary cilia. *Am. J. Physiol. Renal Physiol.* **312**, F96–F108 (2017).
13. X. Liu *et al*., Polycystin-2 is an essential ion channel subunit in the primary cilium of the renal collecting duct epithelium. *eLife* **7**, e33183 (2018).
14. Q. Su *et al*., Structure of the human PKD1-PKD2 complex. *Science* **361**, eaat9819 (2018).
15. M. Wilkes *et al*., Molecular insights into lipid-assisted Ca^{2+} regulation of the TRP channel Polycystin-2. *Nat. Struct. Mol. Biol.* **24**, 123–130 (2017).
16. M. Grieben *et al*., Structure of the polycystic kidney disease TRP channel Polycystin-2 (PC2). *Nat. Struct. Mol. Biol.* **24**, 114–122 (2017).
17. Shen, P. S. *et al*. The structure of the polycystic kidney disease channel PKD2 in lipid nanodiscs. *Cell* **167**, 763–773.e11 (2016).
18. Z. Wang *et al*., The ion channel function of polycystin-1 in the polycystin-1/polycystin-2 complex. *EMBO Rep.* **20**, e48336 (2019).
19. S. Rossetti *et al*.; CRISP Consortium, Comprehensive molecular diagnostics in autosomal dominant polycystic kidney disease. *J. Am. Soc. Nephrol.* **18**, 2143–2160 (2007).
20. N. Hateboer *et al*., Comparison of phenotypes of polycystic kidney disease types 1 and 2. European PKD1-PKD2 study group. *Lancet* **353**, 103–107 (1999).
21. G. Wu *et al*., Somatic inactivation of Pkd2 results in polycystic kidney disease. *Cell* **93**, 177–188 (1998).
22. A. Li *et al*., Human polycystin-2 transgene dose-dependently rescues ADPKD phenotypes in Pkd2 mutant mice. *Am. J. Pathol.* **185**, 2843–2860 (2015).
23. P. Koulen *et al*., Polycystin-2 is an intracellular calcium release channel. *Nat. Cell Biol.* **4**, 191–197 (2002).
24. E. Y. Park *et al*., Cyst formation in kidney via B-Raf signaling in the PKD2 transgenic mice. *J. Biol. Chem.* **284**, 7214–7222 (2009).
25. S. Burtey *et al*., Overexpression of PKD2 in the mouse is associated with renal tubulopathy. *Nephrol. Dial. Transplant.* **23**, 1157–1165 (2008).
26. A. M. Gout, N. C. Martin, A. F. Brown, D. Ravine, PKDB: Polycystic Kidney Disease Mutation DatabaseA gene variant database for autosomal dominant polycystic kidney disease. *Hum. Mutat.* **28**, 654–659 (2007).
27. M. V. Yelshanskaya, S. Mesbahi-Vasey, M. G. Kurnikova, A. I. Sobolevsky, Role of the ion channel extracellular collar in AMPA receptor gating. *Sci. Rep.* **7**, 1050 (2017).
28. C. Lee *et al*., The lysosomal potassium channel TMEM175 adopts a novel tetrameric architecture. *Nature* **547**, 472–475 (2017).
29. S. G. Brohawn, J. del Mármol, R. MacKinnon, Crystal structure of the human K2P TRAAK, a lipid- and mechano-sensitive K+ ion channel. *Science* **335**, 436–441 (2012).
30. V. Hamel *et al*., Correlative multicolor 3D SIM and STORM microscopy. *Biomed. Opt. Express* **5**, 3326–3336 (2014).
31. N. V. Prodromou *et al*., Heat shock induces rapid resorption of primary cilia. *J. Cell Sci.* **125**, 4297–4305 (2012).
32. O. V. Plotnikova, E. N. Pugacheva, E. A. Golemis, Primary cilia and the cell cycle. *Methods Cell Biol.* **94**, 137–160 (2009).
33. P. G. DeCaen, M. Delling, T. N. Vien, D. E. Clapham, Direct recording and molecular identification of the calcium channel of primary cilia. *Nature* **504**, 315–318 (2013).
34. R. E. Hulse, Z. Li, R. K. Huang, J. Zhang, D. E. Clapham, Cryo-EM structure of the polycystin 2-l1 ion channel. *eLife* **7**, e36931 (2018).
35. Q. Su *et al*., Cryo-EM structure of the polycystic kidney disease-like channel PKD2L1. *Nat. Commun.* **9**, 1192 (2018).
36. M. Arif Pavel *et al*., Function and regulation of TRPP2 ion channel revealed by a gain-of-function mutant. *Proc. Natl. Acad. Sci. U.S.A.* **113**, E2363–E2372 (2016).
37. B. Hille, *Ion Channels of Excitable Membranes* (Sinauer, ed. 3, 2001).
38. R. S. Kass, The channelopathies: Novel insights into molecular and genetic mechanisms of human disease. *J. Clin. Invest.* **115**, 1986–1989 (2005).
39. P. Imbrici *et al*., Therapeutic approaches to genetic ion channelopathies and perspectives in drug discovery. *Front. Pharmacol.* **7**, 121 (2016).
40. A. L. George, Jr, Inherited disorders of voltage-gated sodium channels. *J. Clin. Invest.* **115**, 1990–1999 (2005).
41. S. Rossetti *et al*., Incompletely penetrant PKD1 alleles suggest a role for gene dosage in cyst initiation in polycystic kidney disease. *Kidney Int.* **75**, 848–855 (2009). Correction to: Kidney Int. **77**, 368 (2010).
42. H. Wulff, N. A. Castle, L. A. Pardo, Voltage-gated potassium channels as therapeutic targets. *Nat. Rev. Drug Discov.* **8**, 982–1001 (2009).
43. M. de Lera Ruiz, R. L. Kraus, Voltage-gated sodium channels: Structure, function, pharmacology, and clinical indications. *J. Med. Chem.* **58**, 7093–7118 (2015).
44. K. J. Swartz, R. MacKinnon, Mapping the receptor site for hanatoxin, a gating modifier of voltage-dependent K+ channels. *Neuron* **18**, 675–682 (1997).
45. F. Bosmans, K. J. Swartz, Targeting voltage sensors in sodium channels with spider toxins. *Trends Pharmacol. Sci.* **31**, 175–182 (2010).
46. F. Hildebrandt, T. Benzing, N. Katsanis, Ciliopathies. *N. Engl. J. Med.* **364**, 1533–1543 (2011).
47. H. H. Arts, N. V. Knoers, Current insights into renal ciliopathies: What can genetics teach us? *Pediatr. Nephrol.* **28**, 863–874 (2013).
48. H. Seitter, A. Koschak, Relevance of tissue specific subunit expression in channelopathies. *Neuropharmacology* **132**, 58–70 (2018).
49. F. Rubio-Moscardo *et al*., Rare variants in calcium homeostasis modulator 1 (CALHM1) found in early onset Alzheimer's disease patients alter calcium homeostasis. *PLoS One* **8**, e74203 (2013).

50. M. Delling, P. G. DeCaen, J. F. Doerner, S. Febvay, D. E. Clapham, Primary cilia are specialized calcium signalling organelles. *Nature* **504**, 311–314 (2013).
51. M. Delling *et al*., Primary cilia are not calcium-responsive mechanosensors. *Nature* **531**, 656–660 (2016).
52. J. L. Pablo, P. G. DeCaen, D. E. Clapham, Progress in ciliary ion channel physiology. *J. Gen. Physiol.* **149**, 37–47 (2017).
53. H. Tukachinsky, L. V. Lopez, A. Salic, A mechanism for vertebrate hedgehog signaling: Recruitment to cilia and dissociation of SuFu-gli protein complexes. *J. Cell Biol.* **191**, 415–428 (2010).
54. L. Vuolo, A. Herrera, B. Torroba, A. Menendez, S. Pons, Ciliary adenylyl cyclases control the Hedgehog pathway. *J. Cell Sci.* **128**, 2928–2937 (2015).
55. A. Rohou, N. Grigorieff, CTFFIND4: Fast and accurate defocus estimation from electron micrographs. *J. Struct. Biol.* **192**, 216–221 (2015).
56. S. H. Scheres, RELION: Implementation of a Bayesian approach to cryo-EM structure determination. *J. Struct. Biol.* **180**, 519–530 (2012).
57. P. M. Vassilev *et al*., Polycystin-2 is a novel cation channel implicated in defective intracellular Ca(2+) homeostasis in polycystic kidney disease. *Biochem. Biophys. Res. Commun.* **282**, 341–350 (2001).
58. Q. Qian *et al*., Pkd2 haploinsufficiency alters intracellular calcium regulation in vascular smooth muscle cells. *Hum. Mol. Genet.* **12**, 1875–1880 (2003).
59. E. Sammels *et al*., Polycystin-2 activation by inositol 1,4,5-trisphosphate-induced Ca2+ release requires its direct association with the inositol 1,4,5-trisphosphate receptor in a signaling microdomain. *J. Biol. Chem.* **285**, 18794–18805 (2010).
60. Y. Li, J. M. Wright, F. Qian, G. G. Germino, W. B. Guggino, Polycystin 2 interacts with type I inositol 1,4,5-trisphosphate receptor to modulate intracellular Ca2+ signaling. *J. Biol. Chem.* **280**, 41298–41306 (2005).
61. S. Raychaudhuri, Y. J. Im, J. H. Hurley, W. A. Prinz, Nonvesicular sterol movement from plasma membrane to ER requires oxysterol-binding protein-related proteins and phosphoinositides. *J. Cell Biol.* **173**, 107–119 (2006).
62. G. van Meer, D. R. Voelker, G. W. Feigenson, Membrane lipids: Where they are and how they behave. *Nat. Rev. Mol. Cell Biol.* **9**, 112–124 (2008).
63. S. C. Phua *et al*., Dynamic remodeling of membrane composition drives cell cycle through primary cilia excision. *Cell* **168**, 264–279.e15 (2017).
64. F. R. Garcia-Gonzalo *et al*., Phosphoinositides regulate ciliary protein trafficking to modulate hedgehog signaling. *Dev. Cell* **34**, 400–409 (2015).
65. K. R. Laub *et al*., Comparing ion conductance recordings of synthetic lipid bilayers with cell membranes containing TRP channels. *Biochim. Biophys. Acta* **1818**, 1123–1134 (2012).
66. D. Badheka, I. Borbiro, T. Rohacs, Transient receptor potential melastatin 3 is a phosphoinositide-dependent ion channel. *J. Gen. Physiol.* **146**, 65–77 (2015).
67. G. Giebisch, Measurements of electrical potentials and ion fluxes on single renal tubules. *Circulation* **21**, 879–891 (1960).
68. C. Hwang, A. J. Sinskey, H. F. Lodish, Oxidized redox state of glutathione in the endoplasmic reticulum. *Science* **257**, 1496–1502 (1992).
69. J. Birk *et al*., Endoplasmic reticulum: Reduced and oxidized glutathione revisited. *J. Cell Sci.* **126**, 1604–1617 (2013).
70. C. M. Grant, F. H. MacIver, I. W. Dawes, Glutathione is an essential metabolite required for resistance to oxidative stress in the yeast Saccharomyces cerevisiae. *Curr. Genet.* **29**, 511–515 (1996).
71. Y. M. Go, D. P. Jones, Redox compartmentalization in eukaryotic cells. *Biochim. Biophys. Acta* **1780**, 1273–1290 (2008).
72. B. Morgan, M. C. Sobotta, T. P. Dick, Measuring E(GSH) and H2O2 with roGFP2-based redox probes. *Free Radic. Biol. Med.* **51**, 1943–1951 (2011).
73. P. K. Pullela, T. Chiku, M. J. Carvan, 3rd, D. S. Sem, Fluorescence-based detection of thiols in vitro and in vivo using dithiol probes. *Anal. Biochem.* **352**, 265–273 (2006).
74. L. Peng *et al*., Effects of metal ions and disulfide bonds on the activity of phosphodiesterase from Trimeresurus stejnegeri venom. *Metallomics* **5**, 920–927, (2013).
75. I. Y. Kuo *et al*., Polycystin 2 regulates mitochondrial Ca^{2+} signaling, bioenergetics, and dynamics through mitofusin 2. *Sci. Signal.* **12**, eaat7397 (2019).
76. R. Chaube, G. H. Werstuck, Mitochondrial ROS versus ER ROS: Which comes first in myocardial calcium dysregulation? *Front. Cardiovasc. Med.* **3**, 36 (2016).
77. G. Grynkiewicz, M. Poenie, R. Y. Tsien, A new generation of Ca2+ indicators with greatly improved fluorescence properties. *J. Biol. Chem.* **260**, 3440–3450 (1985).
78. C. S. Potter *et al*., Leginon: A system for fully automated acquisition of 1000 electron micrographs a day. *Ultramicroscopy* **77**, 153–161 (1999).
79. D. N. Mastronarde, Automated electron microscope tomography using robust prediction of specimen movements. *J. Struct. Biol.* **152**, 36–51 (2005).
80. S. Q. Zheng *et al*., MotionCor2: Anisotropic correction of beam-induced motion for improved cryo-electron microscopy. *Nat. Methods* **14**, 331–332 (2017).
81. P. Emsley, B. Lohkamp, W. G. Scott, K. Cowtan, Features and development of Coot. *Acta Crystallogr. D Biol. Crystallogr.* **66**, 486–501 (2010).
82. N. Echols *et al*., Graphical tools for macromolecular crystallography in PHENIX. *J. Appl. Cryst.* **45**, 581–586 (2012).
83. C. J. Williams *et al*., MolProbity: More and better reference data for improved all-atom structure validation. *Protein sci.* **27**, 293–315, (2018).
84. E. F. Pettersen *et al*., UCSF ChimeraA visualization system for exploratory research and analysis. *J. Comput. Chem.* **25**, 1605–1612 (2004).